arXiv:1610.00969v1 [cond-mat.mes-hall] 4 Oct 2016

Extracting band structure characteristics of GaSb/InAs core-shell nanowires from thermoelectric properties

Florinda Viñas,[1] H. Q. Xu,[1,2] and Martin Leijnse[1]

[1] *Division of Solid State Physics and NanoLund, Lund University, Box 118, S-221 00, Lund, Sweden*

[2] *Key Laboratory for the Physics and Chemistry of Nanodevices and Department of Electronics, Peking University, Beijing 100871, China*

Nanowires with a GaSb core and an InAs shell (and the inverted structure) are interesting for studies of electron-hole hybridization and interaction effects due to the bulk broken band gap alignment at the material interface. We have used 8-band $\mathbf{k}\cdot\mathbf{p}$ theory together with the envelope function approximation to calculate the band structure of such nanowires. For a fixed core radius, as a function of shell thickness the band structure changes from metallic (for a thick shell) to semiconducting (for a thin shell) with a gap induced by quantum confinement. For intermediate shell thickness a different gapped band structure can appear, where the gap is induced by hybridization between the valence band in GaSb and the conduction band in InAs. To establish a relationship between the nanowire band structures and signatures in thermoelectrical measurements, we use the calculated energy dispersions as input to the Boltzmann equation and to ballistic transport equations, to study the diffusive limit and the ballistic limit respectively. Our theoretical results provide a guide for experiments, showing how thermoelectric measurements in a gated setup can be used to distinguish between different types of band gaps, or tune the system into a regime with few electrons and few holes, which can be of interest for studies of exciton physics.

I. INTRODUCTION

The material system GaSb/InAs is of great interest because it is nearly lattice matched and due to its bulk broken band gap alignment, see Fig. 1(a). The bulk broken band gap alignment leads to a system with hybridizing electron and hole states close to the interface. When confined in a two-dimensional quantum well geometry, the hybridization effect can be large enough that the band structure becomes inverted and gapped at the same time; we call such a band gap a hybridization gap. In this case it has been proven that the GaSb/InAs material system is a topological insulator; it is then the hybridization gap that is responsible for the quantum spin Hall effect.[1] In two dimensions the GaSb/InAs material system may also host excitonic ground states,[2] and in zero-dimensions coupled electron- and hole quantum dots have been studied.[3,4]

Recently it has become possible to grow GaSb/InAs heterostructures in the form of core-shell nanowires.[5–7] A core-shell nanowire[8] is a heterostructure in the radial direction, see Fig. 1(b), with applications within e.g., infrared radiation[9] and energy harvesting.[10] The broken band gap alignment makes GaSb/InAs core-shell nanowires particularly interesting, and recent experiments have shown that the carrier transport can be tuned between hole- and electron dominated by using a gate electrode.[11,12] Previous theoretical studies have investigated the effect of strain in core-shell nanowires of various material combinations[13] and studied the electronic structure of GaSb/InAs core-shell nanowires with strong confinement,[14,15] mainly focusing on tuning the wire dimensions to optimize the hybridization gap.

In this article we present calculations of the band structure and its effect on the carrier transport in GaSb/InAs and InAs/GaSb core-shell nanowires. We focus on conditions that are tractable for epitaxial nanowire growth, meaning a rather thick core radius R_C and growth in the crystallographic [111] direction. We calculate the electronic structure for both GaSb/InAs and InAs/GaSb

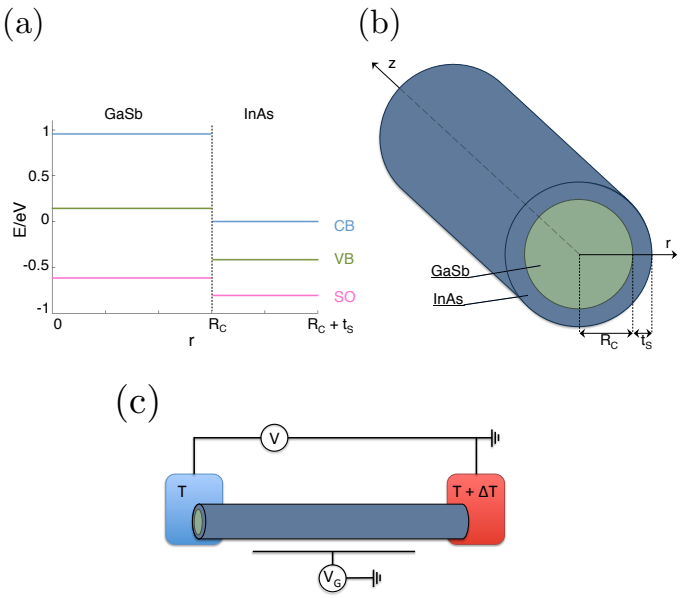

FIG. 1. a) Sketch of the GaSb/InAs bulk band alignment with conduction band edges in blue, valence band edges in green, and split-off band edges in pink. b) Sketch of a cylindrical core-shell nanowire with a GaSb core radius R_C and an InAs shell thickness t_S. c) Sketch showing a setup for transport measurement of a nanowire. Electrodes are depicted in blue and red, with applied source voltage V. The nanowire is subject to a gate voltage V_G and a heat gradient ΔT.

zincblende core-shell nanowires of cylindrical crossections, using 8-band $\mathbf{k}\cdot\mathbf{p}$ theory and the envelope function approximation (EFA), together with a Bessel function basis expansion. In our calculations we focus on nanowires with a fixed core radius $R_C = 20$ nm, and show that hybridization between the valence bands (VBs) and the conduction bands (CBs) occurs, and that by choosing suitable dimensions of the shell thicknesses, a hybridization gap opens up for the nanowires with a GaSb core and an InAs shell. However, for core-shell nanowires with an InAs core and a GaSb shell, there is no shell thickness that gives a hybridization gap for such a large core radius. The transport properties of the core-shell nanowires are studied in two limits; the diffusive limit, employing the semi-classical Boltzmann transport equation, and the ballistic limit. In both these limits, our calculated energy dispersion is used as input, in a similar fashion to Refs. 16–19.

Our results indicate that the presence of a hybridization gap can be deduced from transport properties. Although the conductance looks similar for a nanowire with a hybridization gap and a nanowire with a confinement-induced gap, the two can be distinguished based on the Seebeck coefficient. Similarly, when there is a larger overlap of the GaSb VB and the InAs CB, such that no hybridization gap appears, the thermoelectric transport signatures can reveal the size of this overlap. Therefore, comparing measurements of the Seebeck coefficient with calculated band structures helps to separately determine the electron and hole densities.

The reminder of the paper is organized as follows: Sec. II describes the methods for calculating the band structure and transport properties. Section III presents the results. Finally, Section IV summarizes our findings and concludes.

II. METHOD

A. Electronic structure

In this work we employ the 8-band $\mathbf{k}\cdot\mathbf{p}$ method,[20] commonly referred to as the Kane model, to obtain the electronic dispersion of the nanowires. The $\mathbf{k}\cdot\mathbf{p}$ method is a semi-empirical method to solve the Schrödinger equation to obtain the band structure. Together with the EFA it provides a powerful tool for approximative calculations of the electron energies in low-dimensional structures such as quantum wells, nanowires and quantum dots. For the InAs/GaSb material system it is crucial to use a method such as the 8-band $\mathbf{k}\cdot\mathbf{p}$ method, where the interaction between the CB and the VBs is taken into account.

From the Hamiltonian

$$H = \frac{p^2}{2m_0} + V_0(\mathbf{r}) + \frac{\hbar}{4m_0^2c^2}\mathbf{p}\cdot\sigma\times(\nabla V_0), \tag{1}$$

we can obtain the Kane Hamiltonian H_8, following Refs. 20 and 21. Here $\mathbf{p}$ is the momentum operator, m_0 the electron rest mass, V_0 the periodic crystal potential, c the speed of light, and σ the spin operator. We take one s-like CB and three p-like VBs into account explicitly, using the Bloch function basis

$$\begin{aligned}\{&|S\uparrow\rangle, |P_x\uparrow\rangle, |P_y\uparrow\rangle, |P_z\uparrow\rangle,\\ &|S\downarrow\rangle, |P_x\downarrow\rangle, |P_y\downarrow\rangle, |P_z\downarrow\rangle\},\end{aligned} \tag{2}$$

where S and P refers to the symmetry of the CB and the VBs respectively,[20] and treat coupling to all other bands perturbatively. The 8×8 Kane Hamiltonian can be written as[22,23] $H_8 = H_0 + H_{SO}$ with

$$H_0 = \left(\begin{array}{cc|cc} H_{cc} & H_{cv} & \multicolumn{2}{c}{\multirow{2}{*}{0}} \\ H_{vc} & H_{vv} & & \\ \hline \multicolumn{2}{c|}{\multirow{2}{*}{0}} & H_{cc} & H_{cv} \\ & & H_{vc} & H_{vv} \end{array}\right) \tag{3}$$

and

$$H_{SO} = \frac{1}{3}\Delta_{SO}\begin{pmatrix} 0 & 0 & 0 & 0 & 0 & 0 & 0 & 0 \\ 0 & 0 & -i & 0 & 0 & 0 & 0 & 1 \\ 0 & i & 0 & 0 & 0 & 0 & 0 & -i \\ 0 & 0 & 0 & 0 & 0 & -1 & i & 0 \\ 0 & 0 & 0 & 0 & 0 & 0 & 0 & 0 \\ 0 & 0 & 0 & -1 & 0 & 0 & i & 0 \\ 0 & 0 & 0 & -i & 0 & -i & 0 & 0 \\ 0 & 1 & i & 0 & 0 & 0 & 0 & 0 \end{pmatrix}. \tag{4}$$

Following the Burt-Foreman formalism,[22] the submatrices of H_0 can be expressed as

$$H_{cc} = E_c + k_xAk_x + k_yAk_y + k_zAk_z, \tag{5}$$

$$H_{cv} = \begin{pmatrix} k_yBk_z + iPk_x & k_zBk_x + iPk_y & k_xBk_y + iPk_z \end{pmatrix}, \tag{6}$$

$$H_{vc} = H_{cv}^{\dagger} \tag{7}$$

and

$$H_{vv} = \left(E_v' + \frac{\hbar^2}{2m_0}\mathbf{k}^2\right)\begin{pmatrix}1 & 0 & 0\\ 0 & 1 & 0\\ 0 & 0 & 1\end{pmatrix} \tag{8}$$

$$+\begin{pmatrix}k_xLk_x + k_yMk_y + k_zMk_z & k_xN^+k_y + k_yN^-k_x & k_xN^+k_z + k_zN^-k_x\\ \dagger & k_xMk_x + k_yLk_y + k_zMk_z & k_yN^+k_z + k_zN^-k_y\\ \dagger & \dagger & k_xMk_x + k_yMk_y + k_zLk_z\end{pmatrix} \tag{9}$$

where $E_v' = E_v - \Delta_{SO}/3$. All parameter definitions can be found in Appendix A, and their values are taken from Ref. 24, except P that is calculated according to the formula given by Ref. 22 to avoid spurious solutions. All parameters are assumed to vary step-like at the material interface. We use $N^+ = N^- = N/2$, for a motivation see Appendix A. However, it is worth noting that the ordering of the k operators and the parameter P matters, and that the correct version is indeed given by Eq. (6) and Eq. (7), as suggested by Ref. 22. We assume, like Refs. 15, 22, 25, and 26, that the parameter B in the Kane model can be set to zero when considering a zincblende structure without any external fields.

Choosing z as the nanowire growth direction, we will have

$$k_{r_i} \to -i\frac{\partial}{\partial r_i},\ r_i = x, y \tag{10}$$

while k_z is the crystal momentum in the growth direction. We solve the Schrödinger equation $H_8\psi = E\psi$ using basis function expansion of the envelope functions $\psi(r, \theta, z)$, in a similar fashion to Ref. 27, taking advantage of the rotational symmetry of the cylindrical wire. The expansion we use is given by

$$\psi(r, \theta, z) = \sum_{n=-N}^{N\to\infty}\sum_{l=1}^{L\to\infty} N(n, l)J_n(\alpha_{nl}\frac{r}{R})e^{in\theta}e^{ik_z z} \tag{11}$$

with J_n the first kind Bessel function of order n, α_{nl} its zero of order l, and $N(n, l)$ a normalization factor. The Bessel functions are scaled by the total nanowire radius R.

To be able to make predictions for nanowires grown in the [111] crystallographic direction we must rotate our system. The rotation process is described in detail in Appendix B and follows Refs. 25, 28–30. In addition to the rotation, we follow Refs. 25 and 30 and make a change of basis after the rotation of the Hamiltonian is performed. The new basis $|j, j_z\rangle$, with the total angular momentum j and the angular momentum in the growth axis j_z, diagonalizes the spin-orbit interaction and is also used to label the conduction, heavy hole, light hole and split-off band (see Fig. 1(a)).

B. Transport calculations

We now want to calculate electrical transport through the nanowire as a response to the electrical bias V, with gradient ∇V, and the temperature difference ΔT, with gradient ∇T, see Fig. 1(c). We restrict ourselves to the linear response regime, meaning small V (∇V) and small ΔT (∇T), in which case the current density J becomes

$$J = -\sigma\nabla V - \sigma S\nabla T, \tag{12}$$

where σ is the electrical conductivity and S is the Seebeck coefficient. The corresponding expression for the current is $I = GV + GS\Delta T$, where G is the conductance. The transport calculations are carried out in the limit of diffusive and ballistic transport, with the energy dispersions obtained from the $\mathbf{k}\cdot\mathbf{p}$ calculations as input.

1. *Diffusive transport – the Boltzmann equation*

In the diffusive transport limit, we can find the current density from the distribution function[31] by solving the Boltzmann equation in the linear response regime. Furthermore, we apply the relaxation time approximation and assume that the relaxation time τ is the same for all bands and subbands, and that it is independent of k_z. We then obtain the following expressions for the conductivity and the Seebeck coefficient

$$\sigma = 2e^2\tau\sum_m\int_{-\infty}^{\infty} dk_z v_m^2(k_z)\left(-\frac{\partial f(E_m, E_F)}{\partial E}\right), \tag{13}$$

$$\sigma S = 2eT\tau\sum_m\int_{-\infty}^{\infty} dk_z v_m^2(k_z)(E_m - E_F) \times\left(-\frac{\partial f(E_m, E_F)}{\partial E}\right). \tag{14}$$

Here $-e$ is the electron charge, $f(E_m, E_F)$ is the Fermi-Dirac distribution with Fermi level E_F, T is the temperature, τ is the relaxation time and E_m and $v_m(k_z) = \frac{1}{\hbar}\partial_{k_z}E_m(k_z)$ is the energy and the velocity in band m (by band we mean all one-dimensional subbands seen in Figs. 2 and 3). In general it is not possible to write down these expression as integrals over the energy E_m, unless there exists a function $k_z(E_m)$. The integrals over k_z are

evaluated numerically with our calculated energy dispersion as input.

2. Ballistic transport

In the ballistic limit[32] electrons do not thermalize along the nanowire and one can therefore not define local values or gradients of V and T. Instead the total current is independent of the nanowire length, and depends only on ΔV and ΔT. The conductance and the Seebeck coefficient are then given by

$$G = \frac{e^2}{2\pi}\sum_m \int_{-\infty}^{\infty} \left(-\frac{\partial f(E_m, E_F)}{\partial E}\right) \times \left(v_m^{\rightarrow}(k_z) - v_m^{\leftarrow}(k_z)\right) T(k_z) dk_z \quad (15)$$

$$GS = \frac{e}{2\pi}\sum_m \int_{-\infty}^{\infty} \frac{E_m - E_F}{T} \left(-\frac{\partial f(E_m, E_F)}{\partial E}\right) \times \left(v_m^{\rightarrow}(k_z) - v_m^{\leftarrow}(k_z)\right) T(k_z) dk_z. \quad (16)$$

We will assume that the potential is even along the entire nanowire such that there is no scattering and the transmission coefficient is $T(k_z) = 1$. The velocities $v_{\rightarrow}(k_z)$ and $v_{\leftarrow}(k_z)$ are defined as the carrier velocity for right- and left-moving particles respectively. Here we have used the Kramers degeneracy, $E_+(-k_z) = E_-(k_z)$, so that the first order term vanishes under the k_z-integral when expanding the integrand in a Taylor series. Again, the integration variable k_z cannot be substituted for $E_m(k_z)$, and the integrations must be carried out over k_z.

III. RESULTS

To find the energy dispersion for the core-shell nanowires, we diagonalize the rotated version of H_8 found in Eq. (B7). The energies $E_m(k_z)$ are plotted as a function of k_z.

A. GaSb/InAs

Figure 2 shows band structures for GaSb/InAs core-shell nanowires grown in the [111] direction. The core radius is fixed at $R_C = 20$ nm. The band structures at the energies we focus on are dominated by the VB in GaSb and the CB in InAs. Because of hybridization the bands are far from parabolic, and sometimes vary between positive (CB like) and negative (VB like) for different values of k_z. In Fig. 2(a), the bands overlap completely and no band gap is present, so that the system is metallic. A large number of subbands from the quasi one-dimensional confinement are present, and couplings between bands result in avoided crossings. By decreasing the nanowire shell thickness, a hybridization gap opens up; see Fig. 2(b). In this case we have band inversion together with an effective gap. Just below this

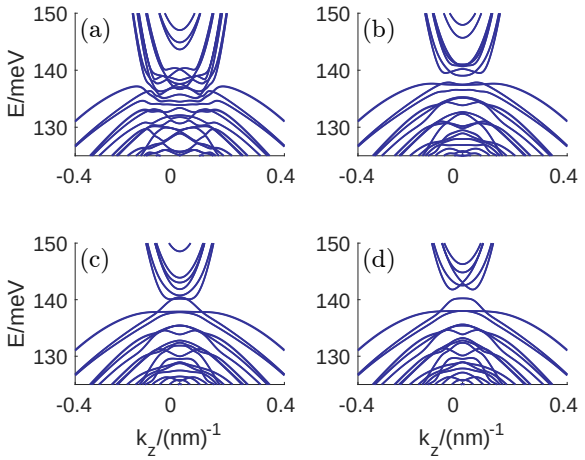

FIG. 2. Band structure for a GaSb/InAs nanowire with core radius $R_C = 20$ nm and shell thickness a) $t_S = 8.5$ nm, b) $t_S = 7.8$ nm, c) $t_S = 7.62$ nm, and d) $t_S = 7.5$ nm. In b) a hybridization gap of 1.1 meV opens up.

hybridization gap a so called "camelback" structure can be seen, where the topmost band has a CB-like appearance around the Γ point, but is VB-like for larger k_z. In Fig. 2(c), the shell thickness is decreased further, leading to a closing of the hybridization gap, so that the system is again metallic. For an even thinner shell, a normal confinement band gap opens up, which can be seen in Fig. 2(d). Both above and below the band gap we see hybridized states, but the camelback feature is not present in the bands closest to the band gap.

These results are qualitatively similar to those for a [001]-wire.[14]

B. InAs/GaSb

Figure 3 shows the calculated band structures for InAs/GaSb core-shell nanowires with core radius $R_C = 20$ nm. In Figs. 3(a) and 3(b), the band structure is ungapped, while in Figs. 3(c) and 3(d) a band gap is present. In contrast to nanowires with GaSb cores we do not observe a hybridization gap for fixed core radius of $R_C = 20$ nm. This difference between nanowires with GaSb- and InAs cores, is a result of the large difference between the effective hole mass in GaSb ($m_{hh} = 0.71 m_0$) and the effective electron mass in InAs ($m_e = 0.026 m_0$). In the GaSb/InAs material system most of the holes are confined in the GaSb and the electrons in the InAs. This means that confinement effects are much less pronounced in GaSb than in InAs, so that for nanowires with an InAs core a very thin GaSb shell is needed to see confinement effects in the shell at all, and the hole energies in this thin shell is then very sensitive to size changes. This leads to the fact that for an InAs/GaSb core-shell nanowire we will have either a confinement gap (for thin shells), or no energy gap at all (for thick shells), but there is no shell

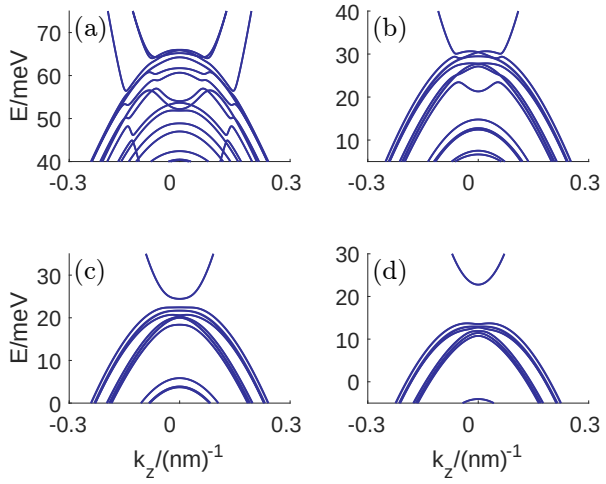

FIG. 3. Band structure for an InAs/GaSb core-shell nanowire with core radius $R_C = 20$ nm and shell thickness a) $t_S = 2.7$ nm, b) $t_S = 2.1$ nm c) $t_S = 2$ nm and d) $t_S = 1.9$ nm.

thickness such that the nanowire exhibits a hybridization gap. However, the band structures for thinner core-shell nanowires (not shown) with InAs cores show qualitatively similar behavior to thinner nanowires with GaSb cores, including the hybridization gap.

C. Transport in core-shell nanowires

Figure 4 depicts the calculated conductivities, conductances and Seebeck coefficients as a function of E_F for the GaSb/InAs core-shell nanowires, corresponding to the band structures in Fig. 2.[33]

A change in E_F can be achieved experimentally by applying a gate voltage. In both the diffusive and the ballistic limit, the calculations are carried out at $T = 1$ K. It is clear that the conductivity, the conductance and the Seebeck coefficient show qualitatively similar behaviors in the diffusive and in the ballistic limit. We note that in both limits the Mott formula[34] gives a reasonable approximation of S (not shown). The relatively larger conductivity in the electron regime in the diffusive limit is a result of the small effective mass associated with the CB, which gives a large mobility in the diffusive limit but has no effect on the conductance in the ballistic limit.

In general an energy gap can be identified from the conductivity or the conductance, by observing where these quantities drop to zero. The conductivities and conductances in Figs. 4(a) and 4(c) are finite for all energies, which confirms that these structures are metallic. For both of the gapped structures, cf. Figs. 2(b) and 2(d), we can similarly confirm the size of the energy gaps by examining the zero conductivities and conductances in Figs. 4(b) and 4(d). An interesting feature of the Seebeck coefficient is that its sign reveals the transport characteristics of the system; a positive (negative) Seebeck coefficient indicates hole (electron) dominated carrier transport.

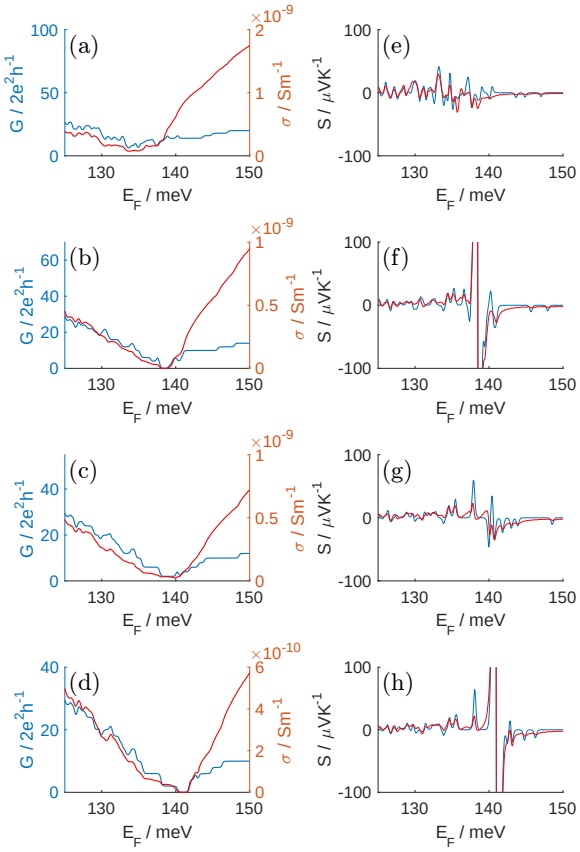

FIG. 4. (a)–(d) Conductivity (red) and conductance (blue), calculated in the diffusive and the ballistic limit respectively, for the GaSb/InAs [111]-nanowires with core radius $R_C = 20$ nm. (e)–(h) Seebeck coefficient, calculated in the diffusive limit (red) and the ballistic limit (blue), for the same wires. (a)–(d) [(e)–(h)] correspond to the nanowire dimensions in Figs. 2(a)–(d).

Based on the conductance trace in Fig. 4(a), it would be difficult to tell whether we have an electron and/or a hole conductor, especially in the ballistic case. However, one sees that S in Fig. 4(e) has both positive and negative peaks for $E_F \lesssim 140$ meV indicating that both electron- and hole-like states contribute to the transport. The absence of hole-like transport, positive peaks in S, for $E_F \gtrsim 140$ meV corresponds to the top of the last VB-like band in Fig. 2(a).

Figures 4(b) and 4(d) show the conductivities and conductances corresponding to the gapped nanowires in Figs. 2(b) and 2(d). Even though there is no qualitative difference between these conductivities, S in Figs. 4(f) and 4(h) differ. In general S for a gapped system always exhibits a large positive peak followed by a large negative peak, indicating hole (electron) dominated transport below (above) the band gap. In Fig. 4(f) we see that S

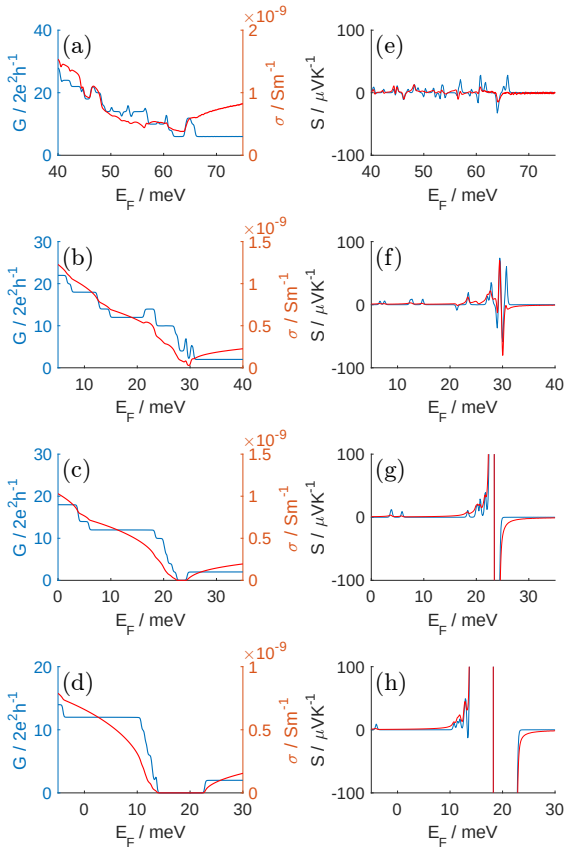

FIG. 5. (a)–(d) Conductivity (red) and conductance (blue), calculated in the diffusive and the ballistic limit respectively, for the InAs/GaSb [111]-nanowires with core radius $R_C = 20$ nm. (e)–(h) Seebeck coefficient, calculated in the diffusive limit (red) and the ballistic limit (blue), for the same wires. (a)–(d) [(e)–(h)] correspond to the nanowire dimensions in Figs. 3(a)–(d).

for the nanowire with a hybridization gap has an additional small negative peak just below the band gap (most clearly seen in the ballistic case). In contrast, in Fig. 4(h), we see that S for the nanowire with a confinement band gap lacks such a negative peak. This negative peak in S, present only for nanowires with a hybridization gap, is even more profound for thinner core-shell nanowires (not shown).

Figure 5 presents the calculated transport properties for a nanowire with an InAs core and a GaSb shell. For such wires, σ and G are less similar than for the inverted structure. From S in Fig. 5(e), we can clearly see that that the VB like bands end at $E_F \approx 65$ meV. For $E_F \gtrsim 65$ meV, we see that $S \approx 0$, corresponding to the lack of CB minima. In Fig. 5(f) it is possible to see where the CB like bands end at just above 20 meV, from studying the sign of S. This feature in S cannot be seen in Figs. 4(e)–(h) or Fig. 5(e) simply because the CBs end at a lower energy than what is visible in the plots. In Figs. 5(g) and 5(h) the appearance of S is typical for a gapped system, with a large positive and a large negative peak around the band gap opening.

IV. CONCLUSIONS

We have used $\mathbf{k}\cdot\mathbf{p}$ theory to determine the band structures for [111] GaSb/InAs and InAs/GaSb core-shell nanowires. The band structures show that by only varying the nanowire shell thickness, the system can be tuned between metallic and insulating, with a tunable band gap for the insulating system. For larger core radii, $R_C \gtrsim 20$ nm, a hybridization gap is present only in GaSb/InAs core-shell nanowires, and not in nanowires with an InAs core. We have used the energy dispersions as input to the Boltzmann equation and to ballistic transport equations to obtain the conductivity and the Seebeck coefficient. The calculated transport properties are similar in both limits, especially for the case with nanowires with GaSb cores. Our results suggest that several band structure features can be seen from the Seebeck coefficient; the highest energy for where we have VB like states, the lowest energy for where we have CB like states, and the presence or absence of a hybridization gap.

ACKNOWLEDGMENTS

The authors would like to thank Stephanie Reimann, Mats-Erik Pistol and Craig Pryor for fruitful discussions. This work was supported by the Swedish Research council (VR), the Crafoord Foundation, the Ministry of Science and Technology of China (MOST) through the National Basic Research Program of China (Grants No. 2012CB932703 and No. 2012CB932700), and the National Natural Science Foundation of China (Grants No. 91221202, No. 91421303, and No. 61321001).

Appendix A: Parameters used in the k · p calculations

The parameters used in the 8-band Kane model are given by:[21,23,29]

$$A = \frac{\hbar^2}{2m_0}(1+2F) \tag{A1}$$

$$P = \sqrt{\frac{\hbar^2}{2m_0}E_P} \tag{A2}$$

$$L = -\frac{\hbar^2}{2m_0}(\gamma_1+4\gamma_2) + \frac{P^2}{E_g} \tag{A3}$$

$$M = -\frac{\hbar^2}{2m_0}(\gamma_1-2\gamma_2) \tag{A4}$$

$$N = -6\frac{\hbar^2}{2m_0}\gamma_3 + \frac{P^2}{E_g} \tag{A5}$$

TABLE I. Numerical values for the parameters used in the $\mathbf{k}\cdot\mathbf{p}$ calculations

	GaSb	InAs
γ_1	13.4	20.0
γ_2	4.7	8.5
γ_3	6.0	9.2
E_g	0.812 eV	0.417 eV
Δ_{SO}	0.76 eV	0.39 eV
m_c	$0.039m_0$	$0.026m_0$

with the Kane energy E_P, the Luttinger parameters γ_1, γ_2 and γ_3 and the band gap E_g. We follow the convention and set $F = 0$. To eliminate spurious solutions, E_P is calculated according to[22]

$$E_P = \frac{3m_0/m_c}{2/E_g + 1/(E_g + \Delta_{SO})} \tag{A6}$$

using the effective electron mass m_c. We use the symmetrization $N^+ = N^- = N/2$, since we have found that for the material system we are solving for, the difference between the symmetrization approach and the Burt-Foreman operator ordering results in a trivially small difference in the [001] direction. The magnitude of this difference is independent of crystal direction,[35] so we can use the symmetrization scheme for a GaSb/InAs core-shell nanowire grown in the [111] direction (or any growth direction) without loss of precision. If this symmetrization scheme for N is imposed, the rotations of the system from the [001] to the [111] crystallographic direction simplifies significantly.

The numerical values for the Luttinger parameters, the band gaps, the split-off band offsets Δ_{SO} and effective electron masses for GaSb and InAs are taken from Ref. 24, and can be found in Table I. The band offset between the VBs of the two different materials are given by $\Delta E = 0.56$ eV.[36–38]

Appendix B: Rotation of the k · p Hamiltonian

For a nanowire grown in another crystal direction than [001] we need to change the basis for the Hamiltonian and rotate our coordinate system. We follow a common approach for this procedure, described in detail by several authors.[25,29,30] The resulting Hamiltonian for the [111] direction is given by

$$\widetilde{H} = Q^* W^* H_0' W^\dagger Q^\dagger + H_{SO}, \tag{B1}$$

where H_0' is the 8×8-Hamiltonian defined in Eq. (3), but with rotated coordinates ($k_i \to k_i'$). The matrix W is a rotation matrix, while the matrix Q accounts for an additional change to the new basis

$$\begin{aligned}\{\, &|S\uparrow\rangle, |S\downarrow\rangle, |HH\uparrow\rangle, |LH\uparrow\rangle, \\ &|LH\downarrow\rangle, |HH\downarrow\rangle, |SO\uparrow\rangle, |SO\downarrow\rangle\}\,.\end{aligned} \tag{B2}$$

The spin-orbit matrix H_{SO} is invariant under rotation, so that it can be taken out of the calculations, together with the diagonal, k-independent part of H. The rotational matrix W is given by

$$W = A\hat{U} \tag{B3}$$

with A defined as

$$A = \begin{pmatrix} \mathrm{e}^{-i\frac{\phi}{2}}\cos\frac{\theta}{2}\mathbb{1}_{4\times4} & \mathrm{e}^{i\frac{\phi}{2}}\sin\frac{\theta}{2}\mathbb{1}_{4\times4} \\ -\mathrm{e}^{-i\frac{\phi}{2}}\sin\frac{\theta}{2}\mathbb{1}_{4\times4} & \mathrm{e}^{i\frac{\phi}{2}}\cos\frac{\theta}{2}\mathbb{1}_{4\times4} \end{pmatrix} \tag{B4}$$

and $\hat{U}$ as

$$\hat{U} = \begin{pmatrix} 1 & 0 & 0 & 0 \\ 0 & U & 0 & 0 \\ 0 & 0 & 1 & 0 \\ 0 & 0 & 0 & U \end{pmatrix} \tag{B5}$$

with

$$U = \begin{pmatrix} \cos\phi\cos\theta & \sin\phi\cos\theta & -\sin\theta \\ -\sin\phi & \cos\phi & 0 \\ \cos\phi\sin\theta & \sin\phi sin\theta & \cos\theta \end{pmatrix}. \tag{B6}$$

The angles ϕ and θ are defined as the azimuthal and the polar angles respectively, by which we rotate our coordinate system. The rotated Hamiltonian for the [111] direction (with N symmetrized and $B = 0$) is given by

$$\widetilde{H} = \left(\begin{array}{c|c|c} H_{CC} & H_{CV8} & H_{CV7} \\ \hline \dagger & H_{V8V8} & H_{V8V7} \\ \hline \dagger & \dagger & H_{V7V7} \end{array}\right). \tag{B7}$$

The submatrices of this rotated Hamiltonian are given by

$$H_{CC} = (E_c + k_x A k_x + k_y A k_y + k_z A k_z)\mathbb{1}_{2\times2}, \tag{B8}$$

$$H_{CV8} = \begin{pmatrix} i\frac{1}{\sqrt{2}}Pk_+ & -i\sqrt{\frac{2}{3}}Pk_z & -i\frac{1}{\sqrt{6}}Pk_- & 0 \\ 0 & i\frac{1}{\sqrt{6}}Pk_+ & -i\sqrt{\frac{2}{3}}Pk_z & i\frac{1}{\sqrt{2}}Pk_- \end{pmatrix}, \tag{B9}$$

$$H_{CV7} = \begin{pmatrix} i\frac{1}{\sqrt{3}}Pk_z & -i\frac{1}{\sqrt{3}}Pk_- \\ i\frac{1}{\sqrt{3}}Pk_+ & i\frac{1}{\sqrt{3}}Pk_z \end{pmatrix}, \tag{B10}$$

$$H_{V8V8} =$$

$$\frac{1}{6}\begin{pmatrix} N(\mathbf{k}^2-3k_z^2) & \frac{1}{\sqrt{3}}[\sqrt{2}(\Gamma_2-N)k_+^2-(2\Gamma_2+N)[k_-,k_z]_+] & \frac{1}{\sqrt{3}}[-(\Gamma_2+2N)k_-^2+\sqrt{2}(\Gamma_2-N)[k_+,k_z]_+] & 0 \\ \dagger & -N(\mathbf{k}^2-3k_z^2) & 0 & -H_{V8V8}(1,3) \\ \dagger & \dagger & -N(\mathbf{k}^2-3k_z^2) & H_{V8V8}(1,2) \\ \dagger & \dagger & \dagger & N(\mathbf{k}^2-3k_z^2) \end{pmatrix},$$

$$+\frac{1}{6}(6E_v'+2\Gamma_1\mathbf{k}^2)\mathbb{1}_{4\times4} \tag{B11}$$

$$H_{V8V7} = \begin{pmatrix} \frac{1}{12\sqrt{3}}\left[-2(\Gamma_2-N)k_+^2+\sqrt{2}(2\Gamma_2+N)[k_-,k_z]_+\right] & \frac{1}{3\sqrt{6}}\left[-(\Gamma_2+2N)k_-^2+\sqrt{2}(\Gamma_2-N)[k_+,k_z]_+\right] \\ \frac{N}{3\sqrt{2}}(\mathbf{k}^2-3k_z^2) & \sqrt{3}H_{V8V7}(1,1) \\ \frac{1}{6}\left[(\Gamma_2-N)k_-^2-\frac{1}{\sqrt{2}}(2\Gamma_2+N)[k_+,k_z]_+\right] & H_{V8V7}(2,1) \\ \frac{1}{3\sqrt{6}}\left[(\Gamma_2+2N)k_+^2-\sqrt{2}(\Gamma_2-N)[k_-,k_z]_+\right] & -\frac{1}{\sqrt{3}}H_{V8V7}(3,1) \end{pmatrix} \tag{B12}$$

and

$$H_{V7V7} = \frac{1}{3}(3E_v'-3\Delta+\Gamma_1\mathbf{k}^2)\mathbb{1}_{2\times2}. \tag{B13}$$

Here, we use the substitution $k_\pm = k_x \pm ik_y$. Terms of the form Dk_i^2 (Dk_ik_j), where D is any parameter, are to be interpreted as k_iDk_i (k_iDk_j) and $\mathbf{k}^2 = k_x^2+k_y^2+k_z^2$. The anti-commutation notation $[k_i,k_j]_+ = k_ik_j+k_jk_i$ is employed, and the substitutions

$$\Gamma_1 = L+2M \tag{B14}$$

$$\Gamma_2 = L-M \tag{B15}$$

are used throughout.

[1] C. Liu, T. L. Hughes, X. L. Qi, K. Wang, and S. C. Zhang, Phys. Rev. Lett. **100**, 236601 (2008).
[2] Y. Naveh and B. Laikhtman, Phys. Rev. Lett. **77**, 900 (1996).
[3] B. Ganjipour, M. Leijnse, L. Samuelson, H. Q. Xu, and C. Thelander, Phys. Rev. B **91**, 161301 (2015).
[4] M. Nilsson, L. Namazi, S. Lehmann, M. Leijnse, K. A. Dick, and C. Thelander, Phys. Rev. B **94**, 115313 (2016).
[5] M. Ek, B. M. Borg, A. W. Dey, B. Ganjipour, C. Thelander, L. E. Wernersson, and K. A. Dick, Cryst. Growth Des. **11**, 4588 (2011).
[6] T. Rieger, D. Grützmacher, and M. I. Lepsa, Nanoscale **7**, 356 (2015).
[7] L. Namazi, M. Nilsson, S. Lehmann, C. Thelander, and K. A. Dick, Nanoscale **7**, 10472 (2015).
[8] L. J. Lauhon, M. S. Gudiksen, D. Wang, and C. M. Lieber, Nature (London) **420**, 57 (2002).
[9] B. Mayer, D. Rudolph, J. Schnell, S. Morkötter, J. Winnerl, J. Treu, K. Müller, G. Bracher, G. Abstreiter, G. Koblmüller, and J. J. Finley, Nat. Commun. **4**, 2931 (2013).
[10] B. Tian, X. Zheng, T. J. Kempa, Y. Fang, N. Yu, G. Yu, J. Huang, and C. M. Lieber, Nature (London) **449**, 885 (2007).
[11] B. Ganjipour, M. Ek, B. Mattias Borg, K. A. Dick, M.-E. Pistol, L.-E. Wernersson, and C. Thelander, Appl. Phys. Lett. **101**, 103501 (2012).
[12] J. G. Gluschke, M. Leijnse, B. Ganjipour, K. A. Dick, H. Linke, and C. Thelander, ACS Nano **9**, 7033 (2015).
[13] M.-E. Pistol and C. E. Pryor, Phys. Rev. B **78**, 115319 (2008).
[14] V. V. R. Kishore, B. Partoens, and F. M. Peeters, Phys. Rev. B **86**, 165439 (2012).
[15] N. Luo, G. Liao, L.-H. Ye, and H. Q. Xu, (2016), arXiv:1603.01020.
[16] J. O. Sofo, G. D. Mahan, and J. Baars, J. Appl. Phys. **76**, 2249 (1994).
[17] T. J. Scheidemantel, C. Ambrosch-Draxl, T. Thonhauser, J. V. Badding, and J. O. Sofo, Phys. Rev. B **68**, 125210 (2003).
[18] A. F. May, D. J. Singh, and G. J. Snyder, Phys. Rev. B **79**, 153101 (2009).
[19] P. D'Amico, L. A. Agapito, A. Catellani, A. Ruini, S. Curtarolo, M. Fornari, M. B. Nardelli, and A. Calzolari, arXiv:1608.05685.
[20] E. O. Kane, J. Phys. Chem. Solids **1**, 249 (1957).
[21] R. Winkler, *Spin Orbit Coupling Effects in Two-Dimensional Electron and Hole Systems* (Springer, New York, 2003).
[22] B. A. Foreman, Phys. Rev. B **56**, R12748 (1997).
[23] S. Birner, *Modeling of Semiconductor Nanostructures and Semiconductor - Electrolyte Interfaces*, Ph.D. thesis (2011).
[24] I. Vurgaftman, J. R. Meyer, and L. R. Ram-Mohan, J. Appl. Phys. **89**, 5815 (2001).
[25] B. Lassen, M. Willatzen, R. Melnik, and L. C. Lew Yan Voon, J. Mater. Res. **21**, 2927 (2006).
[26] R. G. Veprek, S. Steiger, and B. Witzigmann, Phys. Rev. B **76**, 165320 (2007).
[27] D. Gershoni, C. H. Henry, and G. A. Baraff, IEEE J. Quantum Electron. **29**, 2433 (1993).

[28] J. Los, A. Fasolino, and A. Catellani, Phys. Rev. B **53**, 4630 (1996).
[29] M. Willatzen and L. C. Lew Yan Voon, *The kp Method* (Springer, Berlin Heidelberg, 2009).
[30] N. Luo, G. Liao, and H. Q. Xu, (2016), arXiv:1603.00811.
[31] M. Lundstrom, *Fundamentals of Carrier Transport*, 2nd ed. (Cambridge University Press, New York, 2002).
[32] J. H. Davies, *The Physics of Low-Dimensional Semiconductors* (Cambridge University Press, 1998).
[33] In the calculations we use $\tau = 0.5$ ps in rough agreement with Refs. 39 and 40. However, it should be noted that τ only affects the overall magnitude of σ.
[34] M. Cutler and N. F. Mott, Phys. Rev. **181**, 1336 (1969).
[35] B. Lassen, L. C. Lew Yan Voon, M. Willatzen, and R. Melnik, Solid State Commun. **132**, 141 (2004).
[36] A. J. Ekpunobi, Mater. Sci. Semicond. Process. **8**, 463 (2005).
[37] L. M. Claessen, J. C. Maan, M. Altarelli, P. Wyder, L. L. Chang, and L. Esaki, Phys. Rev. Lett. **57**, 2556 (1986).
[38] G. A. Sai-Halasz, L. L. Chang, J. M. Welter, C. A. Chang, and L. Esaki, Solid State Commun. **27**, 935 (1978).
[39] K. Kash, P. A. Wolff, and W. A. Bonner, Appl. Phys. Lett. **42**, 173 (1983).
[40] B. Gonzalez, V. Palankovski, H. Kosina, A. Hernandez, and S. Selberherr, Solid-State Electron. **43**, 1791 (1999).